JOURNAL OF GEOPHYSICAL RESEARCH, VOL. 106, NO. C9, PAGES 19,715–19,729, SEPTEMBER 15, 2001

Observations and modeling of coastal internal waves driven by a diurnal sea breeze

J. A. Lerczak
Department of Physical Oceanography, Woods Hole Oceanographic Institution, Woods Hole, Massachussets, USA

M. C. Hendershott and C. D. Winant
Scripps Institution of Oceanography, University of California, San Diego, La Jolla, California, USA

Abstract. During the Internal Waves on the Continental Margin (IWAVES) field experiments of 1996 and 1997 off of Mission Beach, California (32.75°N), we observed energetic, diurnal-band motions across the entire study site in water depths ranging from 15 to 500 m and spanning a cross-shore distance of 15 km. The spectral peak of the currents was at the diurnal frequency ($\sigma_{D_1} = 1$ cpd) and was sufficiently well resolved to be clearly separated from the slightly higher local inertial frequency ($f = 1.08$ cpd). These motions were surface enhanced and clockwise circularly polarized and had an upward phase propagation speed of $\sim 68\ \mathrm{m\,d^{-1}}$, suggesting that the motions were driven predominantly by the diurnal sea breeze. However, the downward energy (upward phase) propagation seems irreconcilable with the subinertial diurnal period, and moreover, the intermittent diurnal current events were not obviously associated with diurnal sea breeze events. We rationalize these features using a flat-bottomed linear modal sum internal wave model that includes advection and refraction due to subtidal alongshore flow, $V(x,t)$. Fluctuations in V at the observing site can change the "effective" local Coriolis parameter $f + V_x$ by as much as 50%, thus making the diurnal motions at different times effectively either subinertial or superinertial. The model is integrated numerically for 200 days at a latitude of 32.75°N under different wind and subtidal flow conditions: purely diurnal winds and no V, purely diurnal winds and a time-independent V, narrow-band diurnal winds and no V, and narrow-band diurnal winds and subtidal, time-dependent V. Model diurnal currents forced by narrow-band diurnal winds and subtidal V show complex offshore structure with realistic intermittency and spectral broadening. This study suggests that continental margins in the vicinity of the 30° latitude (where $\sigma_{D_i} = f$) are regions that could potentially produce energetic, sea breeze-driven baroclinic motions and that these motions could be regulated by the vorticity of the local subtidal currents.

1. Introduction

During the 1996 and 1997 Internal Waves on the Continental Margin (IWAVES) field studies off of Mission Beach, California, diurnal-band (defined here as between 0.727 and 1.33 cycles per day) currents were energetic, with amplitudes as large as 25 cm $\mathrm{s^{-1}}$. Their structure was similar to that of near-inertial motions observed in the open ocean [*Leaman*, 1976; *Kunze and Sanford*, 1984; *D'Asaro*, 1984] and on continental shelves [*Kundu*, 1976; *Denbo and Allen*, 1984]. Currents were enhanced at the surface and were clockwise polarized (v led u by 90°). Lines of constant phase propagated toward the surface, suggesting a downward energy flux and a surface source for the motions. For this reason, we believe that these motions were not forced by the diurnal surface tide but by the local diurnal sea breeze.

In contrast to near-inertial motions observed elsewhere, current variance observed during IWAVES was not peaked at or slightly above f (1.08 cpd, latitude = 32.75°) but was peaked at the slightly subinertial diurnal frequency ($\sigma_{D_i} = 1$ cpd). In the open ocean and in many coastal regions with strong winds the wind forcing tends to be broad-band, and the nearly resonant inertial frequency is excited more effectively than other frequencies. At the IWAVES study site, however, winds were generally weak but had a sharp peak at σ_{D_i}. Because the wind forcing was predominantly at this single frequency, the response of the ocean was peaked at that frequency.

The strong response of the coastal ocean to the sea breeze during IWAVES remains surprising because σ_{D_i} is slightly subinertial and only a weak evanescent response within the mixed layer would be expected. During IWAVES, however,

Paper number 2001JC000811.
0148-0227/01/2001JC000811$09.00

diurnal currents penetrated considerably below the mixed layer and consistently had an upward phase propagation, which is unexpected for evanescent, subinertial motions. Moreover, diurnal motions were much more intermittent than would be expected for the regular forcing of the sea breeze. Consequently, the diurnal spectral peak of the currents was much broader than the sharp spectral peak of the wind.

We propose that low-frequency background currents play a critical role in setting how effective the sea breeze is at pumping energy into the ocean. A mesoscale eddy field can significantly change the dynamics of near-inertial motions. In particular, the relative vorticity of the eddy field can change the effective Coriolis parameter "felt" by the near-inertial motions, and this can have several results: the horizontal spatial scale of the near inertial motions can be set by the horizontal scale of the eddy field [*Balmforth et al.*, 1998]; the rate of dispersion of near-inertial energy can be enhanced [*Balmforth et al.*, 1998; *van Meurs*, 1998]; trapping and amplification of near-inertial motions can occur in regions of negative relative vorticity [*Kunze*, 1985; *D'Asaro*, 1995]; and spectral broadening of the near-inertial peak can occur due to temporal changes in the background vorticity field [*D'Asaro*, 1995].

Low-frequency currents observed during IWAVES were predominantly oriented in the alongshore direction and had amplitudes as high as 50 cm s^{-1}. The vorticity of these currents V_x changed slowly over time and ranged from $\pm 0.5\, f$. This range was sufficient, at times, to change the effective Coriolis parameter from being subinertial to superinertial and can explain much of the intermittency observed in the diurnal currents.

We begin, in section 2, by giving a brief description of the IWAVES field studies and the data used in these analyses. In section 3 we describe the spatial and temporal structure of the diurnal-band currents observed during IWAVES. In section 4 we describe the alongshore low-frequency currents and their vorticity. In section 5 we summarize the nature of the winds in the vicinity of the IWAVES study site. We conclude that over the cross-shore range of IWAVES (0-15 km from the coast) the diurnal winds were nearly linearly polarized and oriented in the cross-shore direction with a phase that was roughly constant with cross-shore distance. Then, in section 6, we describe a simple linear model with which we attempt to explain some aspects of the diurnal currents observed during IWAVES. In the model, a coastal ocean with a flat bottom is driven by a cross-shore, diurnal wind acting over the mixed layer and decaying away from the coast. A barotropic jet flows in the alongshore direction. The field variables and the forcing are decomposed into vertical modes, and we assume there is no alongshore dependence. First, we describe the case with purely diurnal time dependence. Next, we describe a series of time-dependent simulations in which the diurnal-band winds are comparable to those observed during IWAVES, and the alongshore jet varies in amplitude slowly over time. A comparison of the observed and model diurnal-band currents follows in section 7.

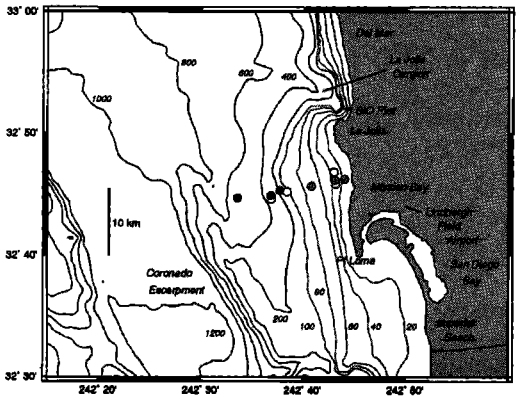

Figure 1. Internal Waves on the Continental Margin (IWAVES) study site. Circles mark the locations of the moorings of the summer arrays (Table 1). Open circles mark moorings deployed in the summer of 1996; solid circles mark summer 1997 moorings; shaded circles mark moorings deployed in the summers of both years. Depths are given in meters. The 1996 and 1997 fall mooring deployments are not shown (see Table 1).

2. Field Studies

During 1996 and 1997, arrays of moorings were deployed off of Mission Beach, California (Figure 1), twice each year with different configurations. From approximately the end of June to the end of August each year, the array spanned depths from 15 to 500 m, covering a cross-shore range of $\sim$ 15 km. During the late summer and early fall, moorings were tightly spaced in shallow, nearshore depths ranging from 15 to 30 m, with the exception of the 100 m mooring deployed in the fall of 1996 (Table 1). This study focuses on data from the broad shelf/slope arrays deployed in the summer and fall of 1996 and the summer of 1997.

Each mooring was instrumented with at least one acoustic doppler current profiler (ADCP) to measure the three components of velocity as a function of depth. On the shelf, between 67 and 80% of the water column was covered by the ADCPs (Table 1). On the slope the full water column could not be sampled because of ADCP range limitations. In 1996 the deeper portion of the water column was sampled at the 350 m mooring. In 1997 two ADCPs (a deep upward looking one and a shallow downward looking one) were deployed on the 350 and 500 m mooring lines. Together they covered approximately the upper 50% of the water column at each mooring. Vertical resolution ranged from 4 to 16 m on the slope and 1 to 4 m on the shelf. Sampling intervals ranged from 1 to 4 min. While not reported on here, several temperature loggers were also deployed on each of the mooring lines.

Wind speed and direction were monitored from the Scripps Institution of Oceanography (SIO) pier ($\sim$ 12 km north of the study site, Figure 1) during the experiments. Wind data were also obtained from the SIO Coastal Data Information Program as well as from National Data Buoy Center (NDBC) and SIO Marine Observatory buoys in the vicinity of the IWAVES study site (Table 2). In addition, con-

Table 1. Parameters of ADCPs Deployed During IWAVES [a]

Mooring Depth, m	Alongshore Direction, deg	ADCP Depth Range, m	Vertical Resolution, m	Sample Time, min	Pings/ Sample	ADCP Frequency, kHz
			Summer 1996			
350	337	151-327	16	4	8	150
100	354	20-88	4	1.5	30	300
70	348	6-62	4	1	24	300
30 c	351	4-24	2	1	30	300
30 n	351	4-24	2	1	30	300
30 s	351	4-24	2	1	30	300
15	360	2-13	1	1	30	1200
			Fall 1996			
100	354	14-90	4	2	32	150
30	351	4-26	2	1	30	300
27.5	353	6-22	2	1	30	300
25	355	6-20	2	1	30	300
22.5	356	5-17	2	1	30	300
20	358	4-14	2	1	30	300
17.5	359	4-12	2	1	30	300
15	360	2-13	1	1	30	1200
			Summer 1997			
500 u	359	17-85	4	1	25	300
500 l		143-279	8	4	13	150
350 u	337	13-89	4	1	25	300
350 l		116-196	4	2	45	300
120	347	24-108	4	2	45	300
30	351	3-27	2	1	40	300
15	360	2-13	1	1	40	1200
			Fall 1997			
30 s	351	4-26	2	2	64	150
30 n	351	3-27	2	1	107	300
25 s	355	4-22	2	1	111	300
25 n	355	4-22	2	1	111	300
20 s	358	2-17	1	2	260	300
20 n	358	2-17	1	2	260	300
15 s	360	1-13	1	2	185	300
15 n	360	2-13	1	1	30	1200

[a]The letters c, n, and s designate moorings deployed at, north of, and south of the central onshore/offshore mooring line. In 1996 north and south moorings at the 30 m isobath were ~1.2 and 0.66 km, respectively, from the center mooring. In 1997 the n and s moorings were separated by 0.5 km. Acoustic Doppler Current Profilers (ADCPs) were at the bottom, looking upward, except that the letters u and l indicate where upper (downward looking) and lower (upward looking) ADCPs, respectively, were deployed on the 500 and 350 m mooring lines in the summer of 1997.

tinuous conductivity-temperature-depth (CTD) yo-yos were conducted at the mooring locations on numerous occasions for periods ranging from 4 to 24 hours.

3. Description of Diurnal Currents

We define the diurnal band as being between 0.727 and 1.33 cpd (1/33 and 1/18 cph). This frequency band includes both σ_{D_i} (1 cpd) and f (1.08 cpd). A 5 day time series of the diurnal-band currents at the 70 and 100 m moorings during the summer of 1996 IWAVES deployment (Figure 2) shows many of the salient features of the diurnal-band currents. Currents were greatest at the surface and decayed with increasing depth. Alongshore currents v led cross-shore currents u by 90°; that is, the currents were clockwise polarized. There was a well-defined upward phase propagation of the currents. The thick dashed lines in Figures 2a and 2b have an upward slope of 50 m d^{-1}. This upward phase propagation is consistent with a downward energy flux and suggests that the source of these motions was at the surface.

3.1. Diurnal-Band Rotary Spectra

Rotary spectra of the currents from the summer of 1997 IWAVES deployment are plotted in Figure 3. The same basic structure was observed in the spectra from the other deployments. To mimimize the spreading of the diurnal frequency into neighboring bins, spectra were calculated using a time block that was a multiple of 24 hours. The full record length of each ADCP time series to within 24 hours was used, and a

Table 2. Wind Stations[a]

Station	Offshore Distance, km	Years Analyzed
NDBC 46047	220	1992-1993, 1999
San Clemente	110	1998-1999
NDBC 46048	60	1992-1993
Pt La Jolla	8	1998-1999
SIO pier	0	1996-1999

[a]Data from buoys NDBC 46047 and NDBC 46048 were obtained from the National Data Buoy Center. San Clemente and Point La Jolla data were from SIO Marine Observatory buoys. The SIO pier data of 1996 and 1997 were from IWAVES observations. The data from 1998 and 1999 were from the SIO Coastal Data Information Program.

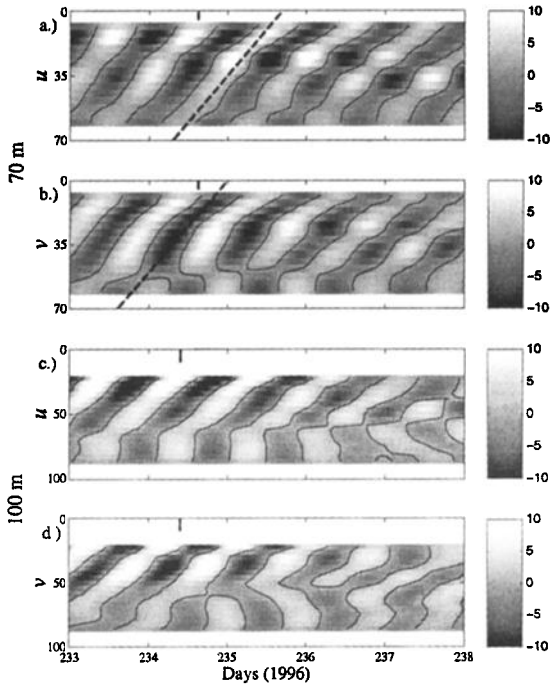

Figure 2. Five day time series of durnal-band (0.727-1.33 cpd) currents versus depth at the 70 and 100 m moorings of the summer of 1996 IWAVES deployment. (a) Cross-shore currents u and (b) alongshore currents v at the 70 m mooring. (c) u and (d) v at the 100 m mooring. The thick vertical lines in Figures 2a and 2b mark a time when the surface u at the 70 m mooring was maximum onshore and the surface v was changing from being northward to southward; that is, the currents were clockwise polarized. The same was true for the currents at the 100 m mooring as indicated by the bold vertical lines in Figures 2c and 2d. The gray scale is in cm s^{-1}. Zero current is indicated by the solid contours. The dashed lines have an upward slope of 50 m d^{-1}.

Hanning window was applied to the time series before calculating the spectra. To maximize the spectral resolution, the spectra were not ensemble averaged in time. Rotary spectra are plotted for five different ADCP bins ranging from near the surface to near the bottom of the water column of each mooring. The range of the diurnal band is marked by the vertical dashed lines in each panel.

For all moorings, clockwise energy (CW) dominated over counterclockwise energy (CCW). Variance within the diurnal band typically decreased with increasing depth. Variance was typically peaked at or near the the diurnal frequency. This result was significant as the vertically averaged, clockwise rotary spectra of all moorings and all deployments (not just those plotted in Figure 3) had peaks at the diurnal frequency and not at the inertial frequency. This was different from the spectral shape often observed for near-inertial motions, for which the peak in energy is at or a few percent higher than the inertial frequency [*D'Asaro et al.*, 1995; *Baines*, 1986]. While energy during IWAVES was typically maximum at the diurnal frequency, the peaks were broad and spanned much of the diurnal band. In Figure 3 this is most evident in the spectra from the 500 m mooring.

3.2. Variance Versus Depth and Cross-Shore Distance

The variance of the diurnal currents, $\langle u^2 \rangle + \langle v^2 \rangle$, typically decreased with depth (Figure 4). The only exception was the shallowest (15 m) mooring of the fall of 1996 (Figure 4b), where the variance near the bottom was as high as that near the surface. In 1996 the variance dropped to < 0.25 its maximum value at a depth of ~ 50 m. In 1997 the variance decreased more slowly with depth. At the 120 m mooring, for example, $\langle u^2 \rangle + \langle v^2 \rangle$ was < 0.25 its maximum value at a depth of ~ 80 m. The variances at the 120 and 350 m moorings in the summer of 1997 (Figure 4c) tracked each other closely with depth. At the 500 m mooring there was a subsurface maximum at a depth of ~ 37 m.

For $H < 100$ m, there was a clear increase in variance with distance from the coast. In the summer of 1996 (Figure 4a), for example, $\langle u^2 \rangle + \langle v^2 \rangle$ near the surface approximately doubled from the 30 to 70 m mooring ($\Delta x = 4.0$ km) and from the 70 to the 100 m mooring ($\Delta x = 3.4$ km).

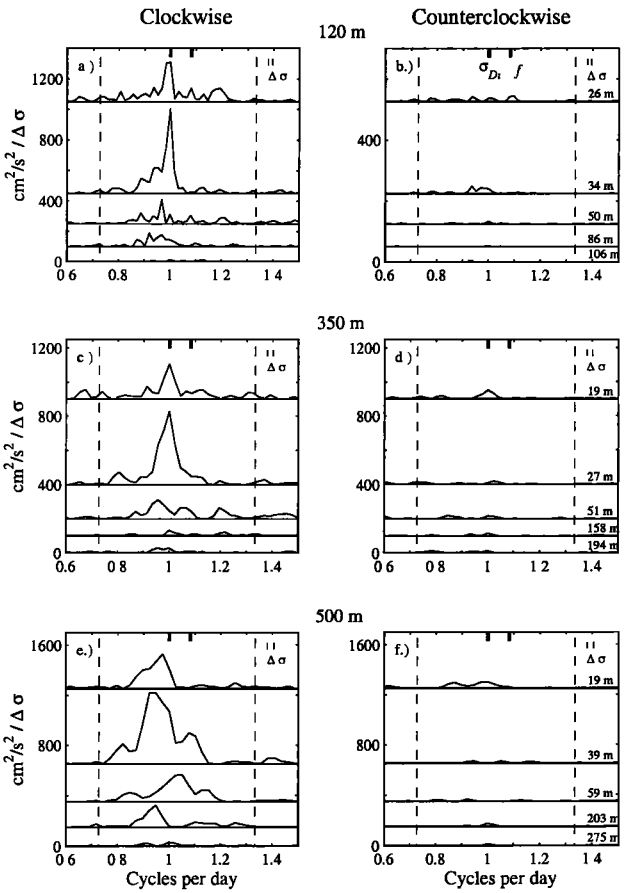

Figure 3. Rotary spectra of diurnal-band currents from the (a-b) 120, (c-d) 350, and (e-f) 500 m moorings of the summer of 1997 IWAVES deployment. The dashed vertical lines mark the frequency range of the diurnal band defined for this study (0.727-1.33 cpd). Spectra are plotted for five ADCP bins for each mooring. Depths of the bins are indicated on the right side of the right panels. The spectral resolution $\Delta\sigma$ of the spectra is indicated at the top right corner of each panel. The diurnal and inertial frequencies are indicated by thick solid lines at the top of each panel.

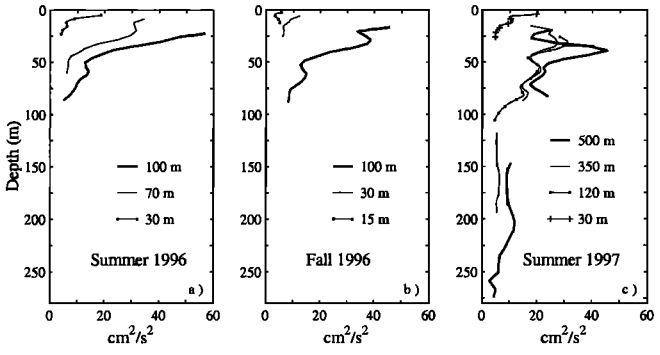

Figure 4. Average diurnal-band variance ($\langle u^2 \rangle + \langle v^2 \rangle$) versus depth at selected moorings of the IWAVES deployments of the (a) summer and (b) fall of 1996 and (c) summer of 1997. The diurnal band is defined as the frequencies between 0.727 and 1.33 cpd.

3.3. Polarization and Ellipticity

The rotary spectra (Figure 3) and 5 day time series (Figure 2) indicate that diurnal CW energy dominates over CCW energy in the diurnal band. To make this assessment more quantitative, we calculated CW/CCW averaged over the upper 50 m of the water column (the depth range over which diurnal band energy tended to be high):

$$\frac{\mathrm{CW}}{\mathrm{CCW}} = \frac{1}{N} \sum_{i=1}^{N} \frac{\mathrm{CW}_i}{\mathrm{CCW}_i}, \qquad (1)$$

where the sum is over the ADCP bins within the upper 50 m of the water column and CW_i and CCW_i are the clockwise and counterclockwise variances at depth bin i, respectively, summed over the diurnal band. For $H \leq 30$ m the sum is over all ADCP bins. Results are summarized in Table 3. For all IWAVES deployments, CW/CCW decreased from the offshore moorings to the coast. For $H > 30$ m, CW/CCW was often > 10, and was between 1 and 2.5 for $H \leq 30$ m.

The square of the ratio of the minor to major diurnal current ellipse axes (ϵ^{-2}) and the major axis orientation (θ) were averaged over the upper 50 m of the water column at each mooring in a similar manner to CW/CCW (Table 3):

$$\epsilon^{-2},\ \theta = \frac{1}{N} \sum_{i=1}^{N} \epsilon_i^{-2},\ \theta_i, \qquad (2)$$

Like CW/CCW, ϵ^{-2} decreased from the offshore moorings to the coast. When the currents were clockwise, circularly polarized (CW/CCW $\gg 1$, $H > 30$ m), $\epsilon^{-2} \to 1$. While the currents at $H \leq 30$ m were clockwise polarized (CW/CCW > 1), they were more elliptical than the currents farther offshore. For the nearshore moorings ($H \leq 30$ m), stable estimates of θ could be obtained, and the major ellipse axis was oriented in the alongshore direction ($\theta \approx 90°$) for all IWAVES deployments.

3.4. Vertical Phase Slope, $\partial\phi_u/\partial z$

Lines of constant phase of the diurnal currents propagated upward in the water column (Figure 2). We have calculated the phase slope ϕ_{uz} versus depth for the cross-shore, diurnal-band currents of the IWAVES moorings. The relative phases $\Delta\phi_{u,i}$ and squared coherence ρ^2 between neighboring ADCP bins were averaged over the diurnal band, and phase slopes were estimated by centered differences. Foward and backward differences were used to calculate ϕ_{uz} at the lowest and uppermost ADCP bins, respectively. Results are summarized in Figure 5.

In the upper 100 m of the water column, ϕ_{uz} was always greater than zero (upward phase propagation) and decreased with increasing depth. In the upper 50 m, where the diurnal currents were most energetic, the average ϕ_{uz} of the six moorings of Figure 5 was $5.3° \mathrm{m}^{-1}$ (vertical dashed line in Figures 5a-5c) corresponding to an upward, diurnal phase speed of $68 \mathrm{m\,d}^{-1}$. Apparently, the phase slope in the upper 50 m was higher during the 1996 deployments (Figures 5a and 5b, average ϕ_{uz} was $6.0° \mathrm{m}^{-1}$) than the summer of 1997 deployment (Figure 5c, average ϕ_{uz} was $4.6° \mathrm{m}^{-1}$).

Below a depth of 100 m (Figure 5c), ϕ_{uz} was somewhat lower than it was higher in the water column. At the 500 m mooring in the summer of 1997, ϕ_{uz} was negative (downward phase propagation) over the depth range 150-210 m.

3.5. Intermittency of the Diurnal Currents

Diurnal current events were very similar at adjacent moorings but were intermittent in time. This is apparent in running estimates of vertically averaged, diurnal-band, horizontal kinetic energy (KE, Figures 6-8), calculated according to

Table 3. Clockwise to Counterclockwise Energy Ratio and Ellipticty of Diurnal-Band Currents[a]

Depth, m	Deployment	$\frac{\mathrm{CW}}{\mathrm{CCW}}$	ϵ^{-2}	θ, deg	Standard Deviation θ, deg	N
15	summer 1996	2.5	0.34	94	4.8	10
15	fall 1996	2.0	0.52	104	15	11
15	summer 1997	1.2	0.29	99	4.2	11
15	fall 1997	2.2	0.39	94	7.6	11
30	summer 1996	2.3	0.52	94	8.0	10
30	fall 1996	2.2	0.61	120	16	11
30	summer 1997	1.6	0.60	99	21	12
30	fall 1997	2.0	0.61	74	14	12
70	summer 1996	15.9	0.90	...	...	...
100	summer 1996	15.7	0.86	...	...	...
100	fall 1996	9.1	0.74	...	...	...
120	summer 1997	6.1	0.73	...	...	...
350	summer 1997	7.6	0.77	...	...	...
500	summer 1997	12.8	0.69	...	...	...

[a]CW/CCW is the ratio of clockwise to counterclockwise energy; ϵ^{-2} is the square of the ratio of the minor to major current ellipse axes; and θ is the orientation of the major ellipse axis (θ) of the diurnal-band currents of the IWAVES deployments. All values were averaged over the ADCP bins within the upper 50 m of the water column. Ellipse orientation is only shown for $H \leq 30$ m. At those mooring locations, ϵ^{-2} was small, and θ was stable over the ADCP bins. The standard deviation of θ is over the number of ADCP bins (N) at each mooring. When the major axis is oriented in the alongshore direction, $\theta = 90°$.

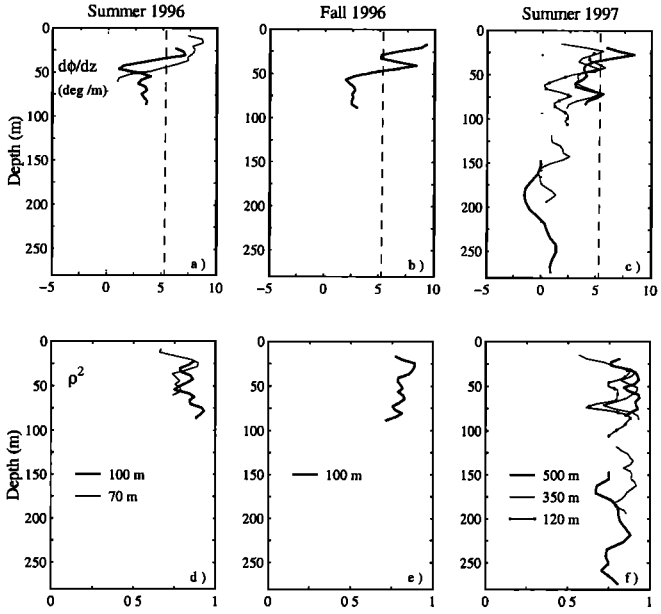

Figure 5. (a-c) Diurnal-band vertical phase slope ϕ_{uz} at selected IWAVES moorings. The vertical dashed lines indicate the ϕ_{uz} (5.3° m^{-1}) averaged over the upper 50 m of the water column and over the six moorings plotted. (d-f) Average diurnal-band coherencies squared (ρ^2) from the neighboring ADCP pairs used to calculate ϕ_{uz}.

$$\mathrm{KE} = \frac{1}{2N}\sum_{i=1}^{N} \langle u^2 \rangle + \langle v^2 \rangle \,, \tag{3}$$

where the sum is over ADCP bins in the upper 100 m of the water column. The temporal averaging, indicated by the angled brackets, was over 2 day time blocks, and an estimate of KE was made every 6 hours.

An increase in KE after day 205 in the summer of 1996 was apparent at the 30, 70 and 100 m moorings (Figure 6a). Modulations of KE with a timescale of $\sim 5-10$ days at the 100 and 70 m moorings tracked each other closely. In the fall of 1996, KE was much higher at the 100 m mooring than at the 30 m mooring (Figure 7a), with three energetic pulses centered at days 264, 280, and 302.

A decrease in diurnal energy toward the coast was also apparent in the KE time series. In the summer of 1997 (Figure 8a), for example, currents were most energetic at the 500 m mooring. The two pulses of enhanced KE centered on days 183 and 208 were apparent for the three moorings plotted. The pulses appeared to propagate offshore. The maximum of the first pulse occurred at day 182.1, 182.6, and 183.15 for the 120, 350, and 500 m moorings, respectively (indicated by the dots above the peaks). The corresponding offshore speeds were 4.8 and 9.7 cm s^{-1} for the 120/350 m and 350/500 m mooring pairs, respectively. Similar offshore speeds were estimated for the second pulse (4.9 and 10 cm s^{-1} for the 120/350 m and 350/500 m mooring pairs, respectively).

4. Low-Frequency Currents and Vorticity

Low-frequency currents ($\sigma < 0.727$ cpd) were predominantly oriented in the alongshore direction during IWAVES. At the 70 m mooring in the summer of 1996, for example, the vertically averaged alongshore variance was 103 cm^2 s^{-2}, while the vertically averaged cross-shore variance was only 5.5 cm^2 s^{-2}. At times, V was effectively barotropic, while at other times, it was sheared in the vertical, with currents flowing in opposite directions at different depths.

We have estimated the vorticity of the low-frequency currents by finite differencing the vertically averaged V between neighboring mooring pairs:

$$V_x = \frac{V_2 - V_1}{\Delta x} \,, \tag{4}$$

where V_i are the vertically averaged V and Δx is the cross-shore separation of the mooring pair. Vertical averaging was done two different ways: over the upper 40 m of the water column and over the upper 100 m of the water column (the entire water column on the shelf). We averaged these two ways to determine how significantly the vertical shear of V affected the estimate of V_x.

In the model we present subsequently, the size of $f + V_x$ relative to f, which we define as Γ $(= 1 + V_x/f)$, is a dynam-

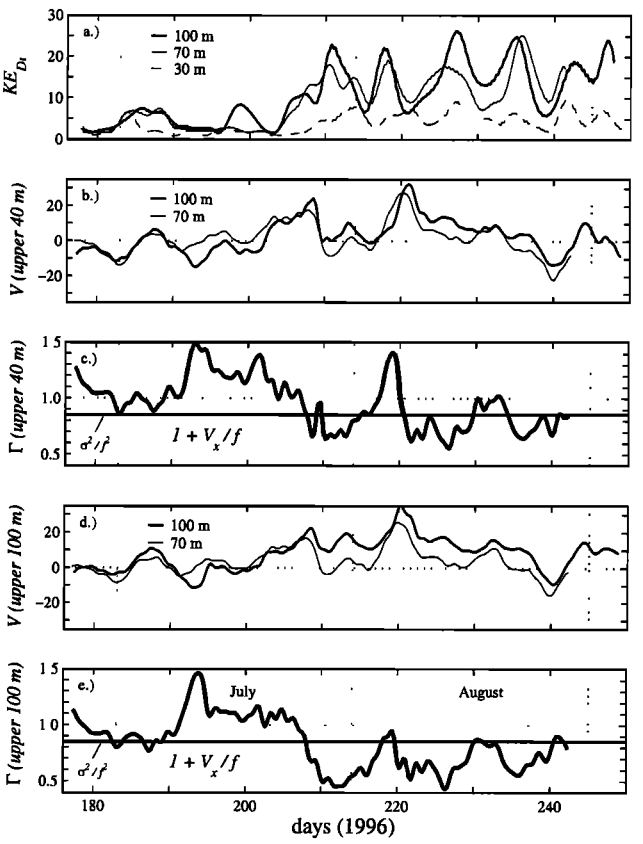

Figure 6. (a) Running diurnal-band kinetic energy vertically averaged over all ADCP bins from the summer of 1996 IWAVES deployment. Running estimates were averaged over time blocks 2 days in length. An estimate was made every 6 hours. (b) Low-frequency, alongshore currents V averaged over the upper 40 m of the water column. (c) $\Gamma = 1 + V_x/f$ with V from Figure 6b. (d) V averaged over the entire water column. (e) $\Gamma = 1 + V_x/f$ with V from Figure 6d. The thick horizontal lines in Figures 6c and 6e mark the value of σ_{Di}^2/f^2 $(= 0.85)$.

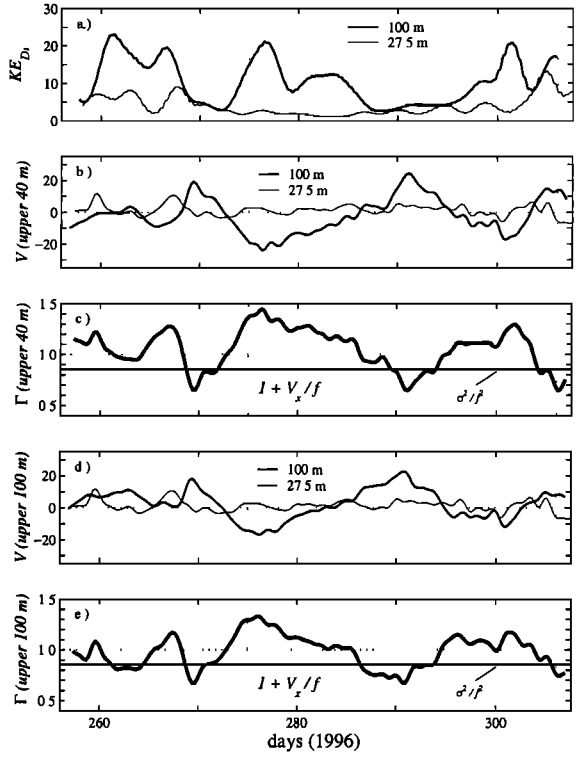

Figure 7. Same as Figure 6, but for the fall of 1996 deployment.

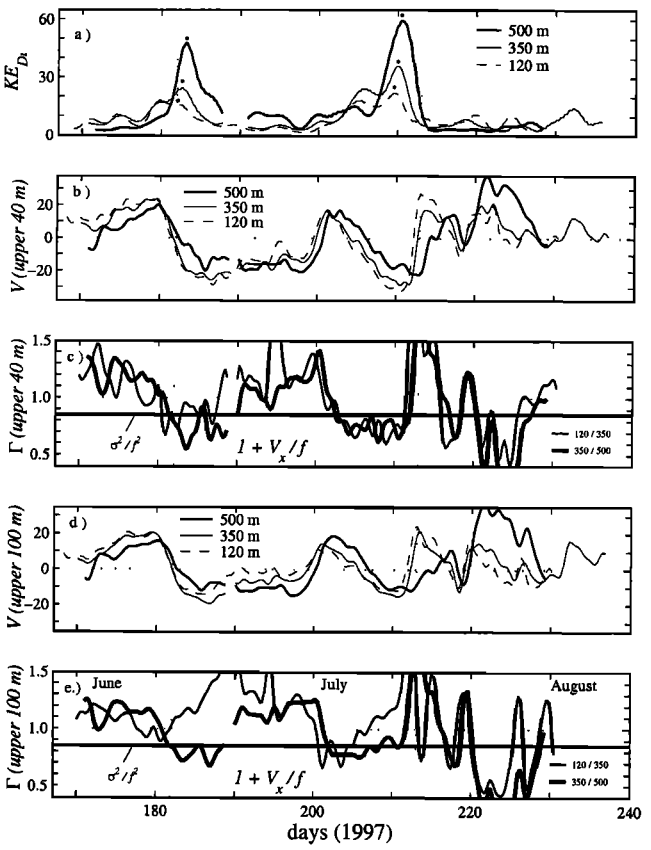

Figure 8. Same as Figure 6, but for the summer of 1997 deployment. At the 500 and 350 m moorings, diurnal KE was averaged over ADCP bins in the upper 100 m of the water column, and V and Γ of Figures 8d and 8e, respectively, were also averaged over the upper 100 m. The dots in Figure 8a indicate the times of maximum KE at the three moorings for the two energetic pulses referred to in the text.

ically important quantity. When $\Gamma > \sigma^2_{D_i}/f^2$ (= 0.85), an evanescent response to the diurnal winds is expected in the coastal ocean, whereas when $\Gamma < \sigma^2_{D_i}/f^2$, diurnal internal waves can be generated by the winds. We plot Γ versus time, estimated for the IWAVES deployments, in Figures 6-8. For these deployments, Γ did not appear to be very sensitive to whether V was averaged over the upper 40 m or the upper 100 m.

In the summer of 1996 (Figures 6c and 6e), Γ, measured between the 70 and 100 m moorings, ranged between 0.8 and 1.5 for the first 30 days of the deployment. At day 208, Γ dropped below $\sigma^2_{D_i}/f^2$ and stayed below for most of the remainder of the deployment. This was particularly evident in Figure 6e. This was the same period when diurnal energy was most energetic (Figure 6a).

In the summer of 1997, Γ dipped below $\sigma^2_{D_i}/f^2$ between days 180-190 and 203-212. This was particularly evident in Figure 8c. These were roughly the same times when the two pulses of enhanced diurnal energy occurred (Figure 8a).

However, coincidence of Γ dropping below $\sigma^2_{D_i}/f^2$ and enhanced diurnal energy did not always occur. For example, in the fall of 1996 (Figure 7), Γ dropped below $\sigma^2_{D_i}/f^2$ twice, around days 269 and 292. In contrast to the summer deployments, diurnal-band energy at the 100 m mooring was relatively low during these two time periods (Figure 7a). In fact, diurnal-band KE was highest during periods when $\Gamma > 1$, e.g., days 260-268, 274-285, and 298-305.

5. Diurnal Winds off of Southern California

Dorman [1982] characterized the winds between San Diego and San Clemente Island (~ 110 km from the coast) using 21 years of measurements from ships and from land stations at the San Diego Airport and the northwest tip of San Clemente Island. We extended the diurnal analysis of *Dorman* [1982] by studying summer wind measurements

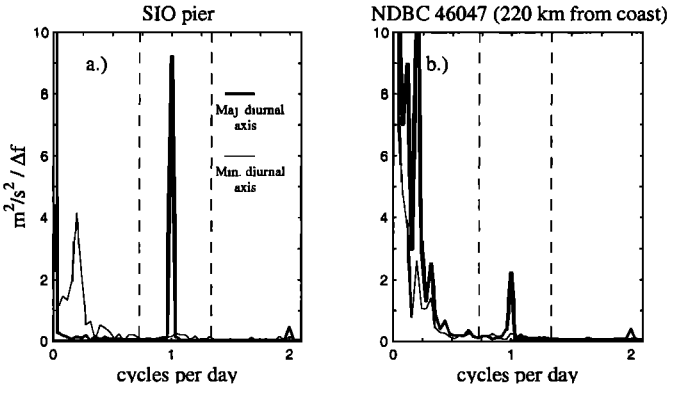

Figure 9. Spectra of wind velocity at the (a) SIO pier and (b) NDBC buoy 46047 in the summer of 1999. Winds were rotated into major (thick line) and minor (thin line) axes of the diurnal-band variance. The major axes were oriented at angles of 106° and 76° relative to true north in Figures 9a and 9b, respectively. The diurnal band, as defined for this study, is indicated by the vertical dashed lines.

obtained from the SIO pier (Figure 1) and various meteorological buoys (Table 2) ranging from a few kilometers from the coast to ~220 km offshore. Details of the analysis are given by *Lerczak* [2000].

Representative wind spectra are shown in Figure 9 (low-frequency variance is plotted in addition to diurnal-band variance). Over the summer months, spectra were averaged over three 25 day long ensembles. The time series were not windowed before calculating the spectra.

The diurnal peaks in the wind spectra were much sharper than the corresponding peaks observed in the current spectra (Figure 3). Diurnal variability was predominantly oriented in the major axis direction; the ratio of major to minor axis variance at the diurnal frequency was 60 at the SIO pier and 8.2 at NDBC 46047. The diurnal-band RMS amplitude, however, was significantly less at NDBC 46047 (0.43 m s^{-1}) compared to the SIO pier (0.88 m s^{-1}).

A running harmonic analysis of the diurnal (24 hour period) winds demonstrates the stability of amplitude and phase over time, especially at the coast. Results for the SIO pier and NDBC 46047 in the summer of 1999 are summarized in Figure 10. At the SIO pier the amplitude of the diurnal winds varied from 0.8 to 1.7 m s^{-1} over the summer (Figure 10a). The phase, however, was remarkably stable over time (Figure 10b). Maximum onshore winds occurred 2.7 hours after local noon. At NDBC 46047 the amplitude of the diurnal winds ranged from 0.25 to 1.25 m s^{-1}, and the phase was somewhat more variable than at the pier. On average, maximum onshore winds at NDBC 46047 occurred 9 hours after local noon (6.2 hours after maximum onshore winds at the SIO pier).

Diurnal-band wind statistics from other years and at other wind stations are summarized in Figure 11. The diurnal-band RMS amplitude of the major ellipse axis winds ranged from 0.4 to 1.1 m s^{-1} (Figure 11a). In 1999 (indicated by stars), winds decayed from the coast to 220 km offshore.

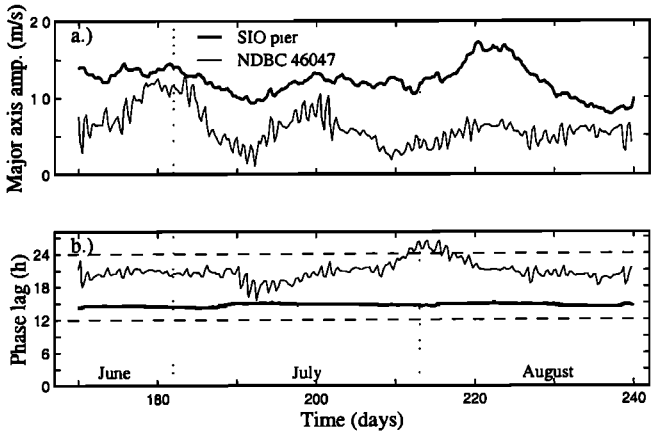

Figure 10. Running estimates of harmonic constants of diurnal (24 hour period) winds at the SIO pier and NDBC buoy 46047 in the summer of 1999. (a) Harmonic amplitude and (b) phase lag were estimated for the major ellipse axis winds using time blocks four days in length. Estimates were made every 6 hours. The phase lag is expressed in hours and is relative to 0000:00 LT.

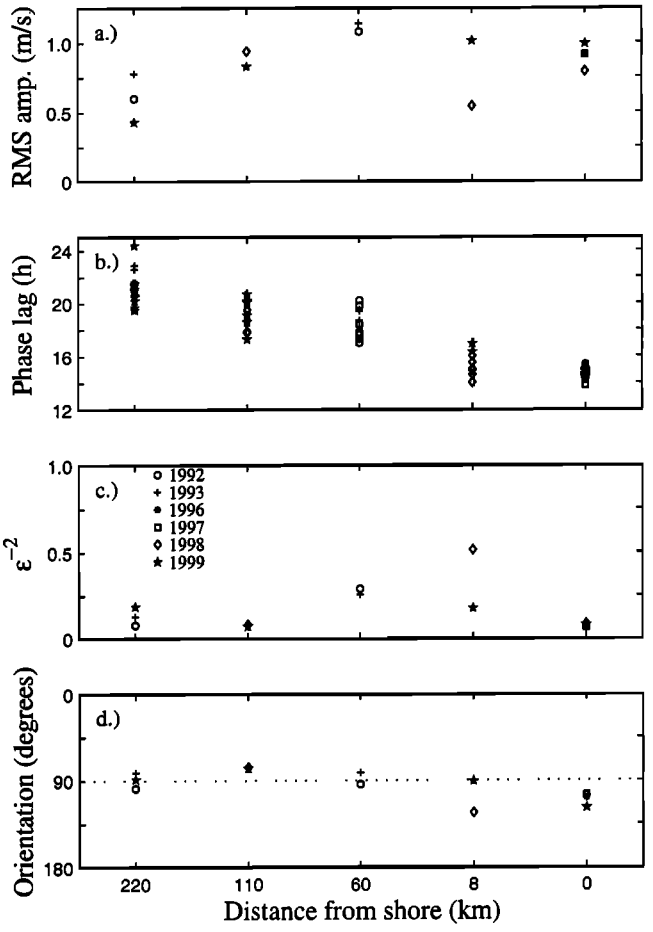

Figure 11. Summary statistics of diurnal-band winds at various stations off the southern California coast (Table 2). (a) RMS amplitude. (b) Relative phase (in hours, relative to 0000:00 LT) calculated from a harmonic analysis of the diurnal (24 hour period) winds using independent time blocks, 8 days in length. Each independent estimate of the relative phase is plotted. (c) Square of the ratio of the minor to major diurnal-band ellipse axes ϵ^{-2}. (d) Orientation of the major ellipse axis, relative to the orientation of the coast (90° is perpendicular to the coast).

However, a trend in the wind amplitude was not obvious for most years studied.

The phase clearly increased from the coast to 220 km offshore (Figure 11b). On average, the time of maximum onshore winds was 6.6 hours later 220 km offshore than at the coast.

At all stations, diurnal winds were highly elliptical (Figure 11c). The square of the ratio of minor to major ellipse axes ϵ^{-2} was usually < 0.25. At the SIO pier (0 km from the coast) the average ϵ^{-2} over the four summers sampled was 0.07. The orientation of the major axis was scattered around 90° (Figure 11d); that is, winds were approximately normal to the coast. From this analysis we conclude that, over the extent of the IWAVES array, diurnal winds were coherent, had nearly a constant phase, and were nearly linearly polarized in the cross-shore direction.

6. Modeling a Sea Breeze-Driven Coastal Ocean

We explain some of the features of the diurnal currents observed during IWAVES using a variation of the model described by *Gill and Clarke* [1974] and used with modifications by *Zervakis and Levine* [1995] and *Balmforth and Young* [1999]. The geometry is shown in Figure 12. A straight coastline ($x = 0$) runs parallel to the y axis, and a continental shelf with constant depth H extends to the west. A slowly varying, barotropic geostrophic current, $V(x,t)$, flows parallel to the coast. All field variables are assumed to be independent of y. We consider only the cross-shore wind stress with a predominantly diurnal frequency.

The model equations are linear, hydrostatic, and Boussinesq with rotation and wind forcing:

$$u_t - fv = -\pi_x + X_z\,, \tag{5}$$

$$v_t + f(1 + \frac{V_x}{f})u = 0\,, \tag{6}$$

$$N^2 w = -\pi_{zt}\,, \tag{7}$$

$$u_x + w_z = 0\,. \tag{8}$$

The variable π is the pressure perturbation divided by the mean density, (u,v,w) are velocity components in the (x,y,z) directions, and f is the local Coriolis parameter. The ocean is forced by a prescribed wind stress, $X(x,z,t)$, acting over the mixed layer. We assume the wind blows only in the x direction.

Like *Gill and Clarke* [1974], we assume all field variables (including the wind forcing) are separable in the horizontal and vertical coordinates and decompose them into normal modes:

$$u,\ v,\ \pi\,, X_z = \sum_{n=0}^{\infty}\{u_n(x,t),\ v_n(x,t),\ p_n(x,t),\ \alpha_n\chi(x,t)\}\,\psi_n(z)\,, \tag{9}$$

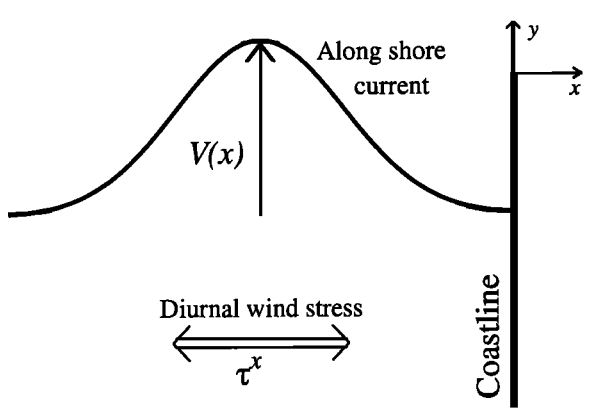

Figure 12. Schematic of the model. A straight coastline runs parallel to the y axis, and a continental shelf with constant depth H extends to the west. A slowly varying geostrophic current, $V(x,t)$, flows parallel to the coast. This flow is assumed to be independent of y.

$$w = \sum_{n=0}^{\infty} w_n(x,t)\phi_n(z)\,. \tag{10}$$

Separability requires that the vertical structure functions (ψ_n and ϕ_n) are related by

$$\phi_{nz} = \psi_n \qquad -\frac{N^2}{{c_n}^2}\phi_n = \psi_{nz}\,, \tag{11}$$

where c_n is a separation constant with units of wave speed. These relationships lead to the eigenvalue equation,

$$\phi_{nzz} + \frac{N^2}{c_n^2}\phi_n = 0\,. \tag{12}$$

Rigid-lid, flat-bottomed boundary conditions ($\phi_n = \psi_{nz} = 0$ at $z = 0, -H$) are assumed, and the normalization of ψ_n is defined by

$$\frac{1}{H}\int_{-H}^{0} \psi_n^*\psi_m\, dz = \delta_{nm}\,, \tag{13}$$

where δ_{nm} is the Kronecker delta and the asterisk indicates complex conjugation. The coefficients α_n that couple the wind to the nth internal wave mode are therefore given by

$$\alpha_n\chi(x,t) = \frac{1}{H}\int_{-H}^{0} \psi_n^* X_z\, dz\,. \tag{14}$$

The resulting equations for u_n, v_n, and p_n are

$$u_{nt} - fv_n = -p_{nx} + \alpha_n\chi\,, \tag{15}$$

$$v_{nt} + f\Gamma u_n = 0\,, \tag{16}$$

$$p_{nt} + {c_n}^2\, u_{nx} = 0\,, \tag{17}$$

where $\Gamma = 1 + V_x/f$. From (15)-(17) a single equation for u_n can be obtained:

$${c_n}^2\partial_{xx}u_n - (\partial_{tt} + f^2\Gamma)u_n = -\alpha_n\partial_t\chi\,. \tag{18}$$

6.1. Stratification

The model buoyancy frequency profile (Figure 13a) is similar to that observed in the upper 100 m off of Mission Beach during IWAVES:

$$N(z) = N_o\,\frac{1}{2}\left[1 + \tanh(\frac{z - z_m}{\epsilon})\right]\left[1 + e^{\frac{z - z_o}{\delta}}\right]\,. \tag{19}$$

This profile has a mixed layer of thickness z_m, rises to a maximum value at the base of the mixed layer, and decays exponentially below. To match conditions at Mission Beach, we take $N_o = 5.12\text{x}10^{-3}$ s^{-1}, z_m = -10 m, z_o = -40.7 m, δ = 15.6 m, and ϵ = 2 m. The maximum N (period = 3.1 min) occurs at a depth of 12.8 m. The buoyancy period at the seafloor is 20 min (Figure 13a).

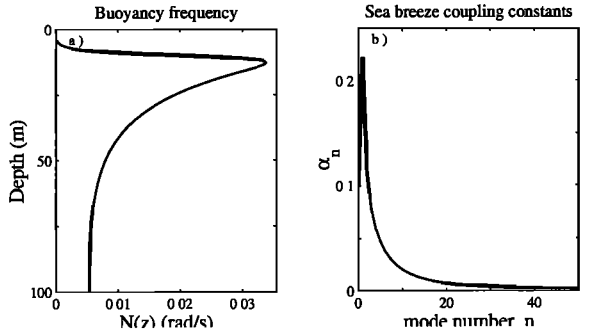

Figure 13. (a) Buoyancy frequency profile used in the model. (b) Coupling constants α_n of the model wind to the nth internal wave normal mode.

6.2. Coupling to the Wind

How the wind couples to the different internal wave modes depends on the underlying stratification, which defines the vertical structure of the internal wave modes and the structure of the wind-driven Ekman layer. As in *Gill and Clarke* [1974] and *Balmforth and Young* [1999], we assume the sea breeze forcing acts predominantly in the surface mixed layer, and we give it the following form:

$$X_z = \frac{1}{2}\left[1 + \tanh\left(\frac{z - z_m}{\epsilon}\right)\right] \chi(x,t) \qquad (20)$$

$$\chi = \frac{1}{\rho_o}\frac{\tau^x(x,t)}{z_m}\,. \qquad (21)$$

The resultant coupling constants α_n decay rapidly with mode number (Figure 13b). For analytical convenience, we consider a wind that decays exponentially away from the coast, $\chi \sim e^{\mu x}$.

6.3. Exactly Periodic Solutions

Consider the long time response of the ocean to a sea breeze with a single frequency σ when the background flow is steady. Assume that all transients have propagated away from the vicinity of the coast, and that the ocean oscillates with the same frequency as the wind ($u_n \sim e^{-i\sigma t}$). Equation (18) becomes

$$u_{nxx} + \frac{\sigma^2 - f^2\Gamma}{{c_n}^2}\, u_n = \frac{i\sigma}{{c_n}^2}\alpha_n \chi\,. \qquad (22)$$

When there is no background flow ($\Gamma = 1$), we can solve for u_n analytically. At the coast, u_n goes to zero, and a radiation condition is imposed at $x \to -\infty$; that is, either the solution decays away from the coast, or waves are allowed to propagate away from but not towards the coast. The solution is

$$u_n = \alpha_n \frac{i\sigma}{{c_n}^2}\frac{1}{\rho_o}\frac{{\tau_o}^x}{z_m}\frac{1}{\kappa_n^2 + \mu^2}\left(e^{\mu x} - e^{-i\kappa_n x}\right), \qquad (23)$$

where $\kappa_n^2 = (\sigma^2 - f^2)/c_n^2$.

The diurnal wind stress at the coast, τ_o^x, was estimated to be $\rho_{\text{air}} C_D U^2$, where ρ_{air} is the density of air (1.2 kg m^{-2}), C_D is a drag coefficient (1.1x10^{-3}), and U is the amplitude of the sea breeze at the coast (1.5 m s^{-1}). Using these values, $\tau_o^x = 0.03$ dyn cm^{-2}. We calculated the purely diurnal solution for a sea breeze decay scale μ^{-1} of 50 km at latitudes where the diurnal frequency is superinertial (29.5°) and subinertial (32.75°) (Figure 14). The subinertial latitude is the same latitude as the IWAVES experiments. The ocean's response near the coast is not very sensitive to μ. The first 100 vertical modes were solved for in the calculation. When the diurnal frequency is superinertial, a beam of internal waves radiates away from the coast along an internal wave characteristic (dashed line) starting at the base of the mixed layer (Figures 14a and 14b). Maximum currents in the beam are 14 cm s^{-1}. At a distance of 5 km from the coast (Figure 14d), there is a sharp phase shift in the cross-shore currents u at the base of the mixed layer. The currents directly responding to the wind in the mixed layer have a constant phase with depth. At a distance of 40 km from the coast, currents have a higher amplitude than closer to the

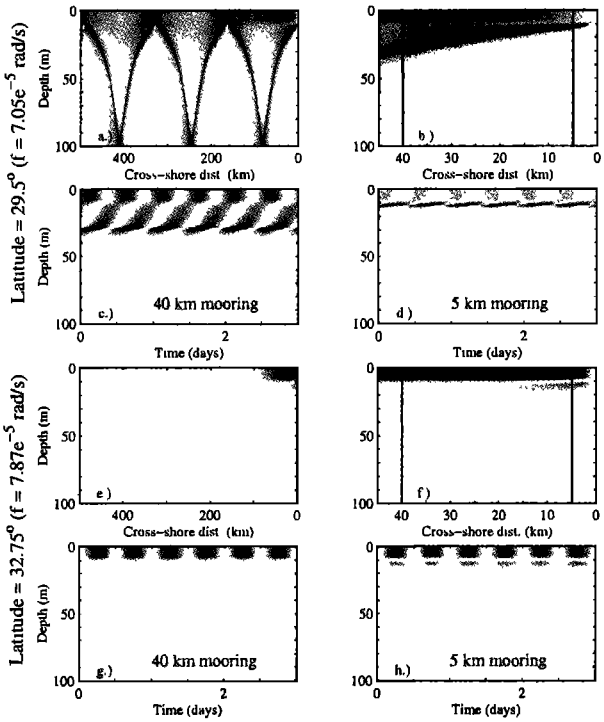

Figure 14. Model solutions of u^2 for a purely diurnal-dependent sea breeze-driven coastal ocean (summation of 100 vertical modes of (23)). The sea breeze frequency is 1 cpd, its offshore decay scale μ^{-1} is 50 km, and its amplitude at the coast is 1.5 m s^{-1}. The ocean's response was calculated at (a-d) a latitude of 29.5° and (e-h) 32.75° (the latitude of the IWAVES field study). Figures 14a and 14e show u^2 versus cross-shore distance and depth. Figures 14b and 14f are the same as Figures 14a and 14e but for the first 45 km from the coast. The thick vertical lines indicate the locations of synthetic moorings. Figures 14c, 14d, 14g, and 14h show u^2 versus time and depth at the two synthetic moorings. The gray scale is 0 – 50 cm^2 s^{-2} for Figures 14a-14d and 0 – 1 cm^2 s^{-2} for Figures 14e-14h. The dashed line in Figure 14a indicates the diurnal characteristic emanating from the coast.

coast. The mixed layer currents have a constant phase with depth, while the phases in the beam below the mixed layer propagate upward. The width of the beam extends from the base of the mixed layer to 40 m below the surface.

At the subinertial latitude (Figures 14e-14h), currents are much weaker; the maximum amplitude of u is 1 cm s^{-1}. Within the mixed layer, currents decay offshore with the decay scale of the sea breeze. There is a 180° phase shift in the currents at the base of the mixed layer. The currents just below the mixed layer occur because of the coastal boundary condition. Their offshore decay scale is the deformation radius of the first internal wave mode (c_1/f, 6.1 km in this case).

6.4. Exactly Diurnal Response with $\Gamma \neq 0$

The parameter $\Gamma - 1$ is the ratio of the relative vorticity of the background current to the planetary vorticity f. This relative vorticity changes the effective Coriolis constant felt by the diurnal motions [*Kunze*, 1985; *D'Asaro*, 1995; *Balmforth and Young*, 1999]. When $\Gamma > \sigma^2/f^2$, (22) is elliptic in (x,z). The ocean's response will be evanescent as in the subinertial case of Figures 14e-14h. However, when $\Gamma < \sigma^2/f^2$, (22) is hyperbolic in (x,z), and internal waves will freely propagate.

To demonstrate this, we solved (22) with a Gaussian jet flowing in the alongshore direction (Figure 15a):

$$V = V_o e^{-\frac{1}{2}\left(\frac{x-x_o}{\lambda}\right)^2}. \qquad (24)$$

In all subsequent analyses, $V_o = 40$ cm s^{-1}, $x_o = -25$ km, and $\lambda = 10$ km. The resulting Γ is shown in Figure 15b. Over the cross-shore range 5.4-22 km from the coast, $\Gamma < \sigma^2/f^2$.

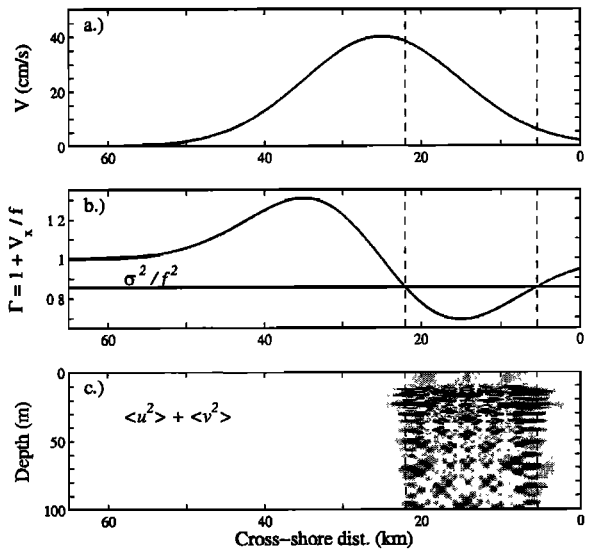

Figure 15. (a) Cross-shore profile of the alongshore jet used in the model. The jet is Gaussian in shape, centered at 25 km offshore, with a width of 20 km. The maximum amplitude is 40 cm s^{-1}. (b) The resultant Γ from the jet. (c) $\langle u^2 \rangle + \langle v^2 \rangle$ from the purely diurnal model solution of (22) with a diurnal wind forcing and the Γ of Figure 15b. The model was calculated for a latitude of 32.75°.

We solved (22) numerically for the first 50 modes using the generalized method of Gaussian elimination described by *Lindzen and Kuo* [1969] with a zero cross-shore flow boundary condition at the coast and a radiation boundary condition 1000 km offshore. The latitude was set to 32.75°, the same as the location of IWAVES. The variance of the currents as a function of cross-shore distance and depth is plotted in Figure 15c. Outside of the range where $\Gamma < \sigma^2/f^2$, the variance is low. The two locations where $\Gamma = \sigma^2/f^2$ (vertical dotted lines) act as caustics for internal wave reflection. Where $\Gamma < \sigma^2/f^2$, an energetic, complicated internal wave pattern occurs, with beams being reflected off the bottom and at the base of the mixed layer.

6.5. Time-dependent Wind and V

In the above, we assumed that there is no time dependence to the background currents and that the wind blows purely at the diurnal frequency. Consequently, high modes were present in the solutions, resulting in complicated spatial patterns of the internal wave field (Figure 15c). However, high modes travel slowly, and in a time-dependent background field they would probably not have time to evolve and make a coherent contribution to the solution. For example, consider the time it would take a particular mode to propagate across the region where $\Gamma < \sigma^2/f^2$ in Figure 15b ($\Delta t = \Delta x/c_n$). For the first mode, Δt is ~ 0.5 days. For the 50th mode, Δt is ~ 30 days, longer than the timescale of variability of V during the IWAVES experiments (Figures 6 to 8). Therefore, for realistic variability in V we need to study the time-dependent problem.

We solved (15)-(17) numerically with a time-dependent Γ and realistic diurnal-band wind variability at the same latitude as IWAVES. The equations were finite differenced over a 400 km domain in the cross-shore direction. An Adams-Bashforth time stepping scheme was used to integrate the equations forward in time, and the time step was made short enough so that the Courant-Friedrichs-Lewy stability condition was met for all vertical modes solved for. A sponge layer was added to the offshore end of the domain.

The model winds were constructed to have the statistical variability of the diurnal-band winds observed during IWAVES (Figure 9a). The winds were peaked at the diurnal frequency with a uniform, low background level across the diurnal band. In order to avoid generating large transients at the start of a model run, we ramped the winds up from zero amplitude to a final stationary amplitude of 1.5 m s^{-1} over the first 20 days (Figure 16a). As before, the winds were given an offshore decay scale of 50 km.

The background jet V had the shape shown in Figure 15a, but its amplitude V_o was modulated over time. Three simulation cases were run. In case I the jet amplitude was set to zero for the entire simulation. In case II (Figure 16e), V_o was set to zero for the first 50 days and was then ramped up over the next 10 days to a maximum northward amplitude of 40 cm s^{-1}. The jet remained with this amplitude for the next 70 days and was then ramped down to zero over a period of 10 days. It remained at zero for the rest of the simulation. Like case II, V_o of case III was set to zero for the first 50 and

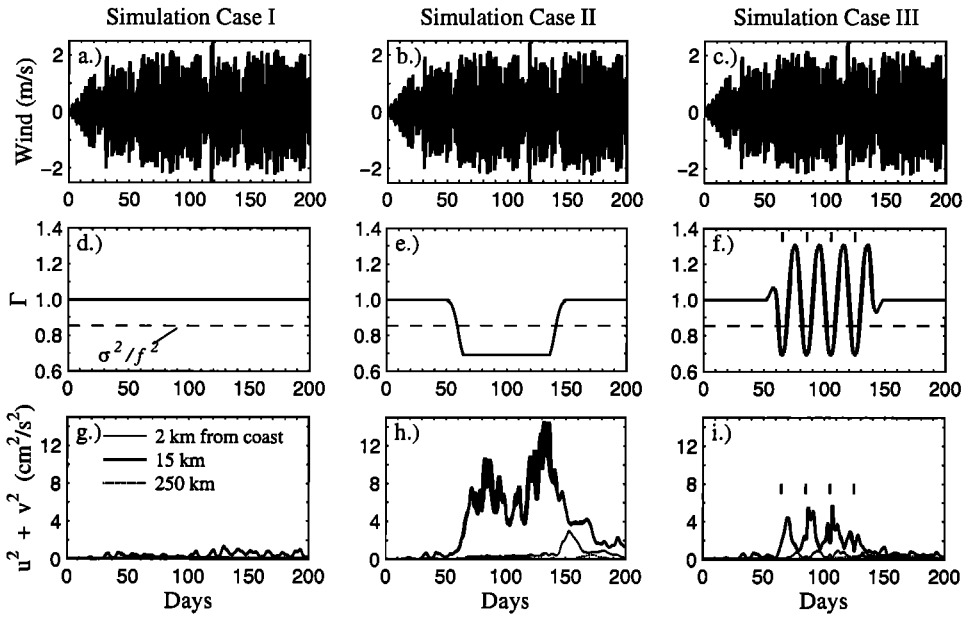

Figure 16. Time series from three time-dependent simulation cases. (a-c) Cross-shore wind at the coast. The winds decayed offshore with a decay scale of 50 km. (d-f) Γ at 15 km from the coast (Figure 15b). (g-i) Vertically averaged $u^2 + v^2$ at different cross-shore locations.

last 50 days (Figure 16f). From days 50 to 150, however, V_o oscillated about ± 40 cm s^{-1} with a period of 20 days. All simulations were run for 200 days and the first 25 modes.

We consider the response of the ocean at three different locations from the coast: 2 km (inshore of the region where Γ can be less than σ^2/f^2), 15 km (the location with the lowest value of Γ when the jet flows northward), and 250 km (beyond the influence of the wind and the jet). The vertically averaged variance ($u^2 + v^2$) versus time is plotted for the three offshore locations and three simulation cases in Figures 16g-16i.

When $\Gamma = 1$ (case I), the variance was low at all three locations (Figure 16g) but was highest 15 km from the coast. There the variance increased slowly over the first 20 days (the period over which the winds were ramped up). Afterward, the variance was modulated over time but apparently remained at a stationary level. The modulation in the variance was apparently due to the modulation of the diurnal wind.

Over the first 45 days, case II (Figure 16h) was identical to case I. Once the jet was turned on at day 50, however, the variance rapidly increased at the 15 km location. A slight rise in the variance at the 2 km location was also apparent. After day 145, when V was ramped down, the variance at 15 km gradually decayed. The variance at 2 km rose abruptly at day 155, apparently the result of internal wave energy being released from the trapping region. A slight rise in variance at the 250 km location occurred at day 170 and was apparently due to internal wave energy radiating away from the coast.

In case III (Figure 16i) the rise in variance at 15 km was not as dramatic as in case II. Pulses in variance occurred $\sim$ 5 days after maximum northward V. Peaks in the variance at 2 km occurred roughly at the time of the minima in variance at 15 km. The variance at 250 km rose at about day 100 and remained comparatively high until about day 180, again apparently due to the radiation of internal waves away from the coast.

Vertically averaged, clockwise polarized spectra at the three cross-shore locations are plotted in Figure 17. Coun-

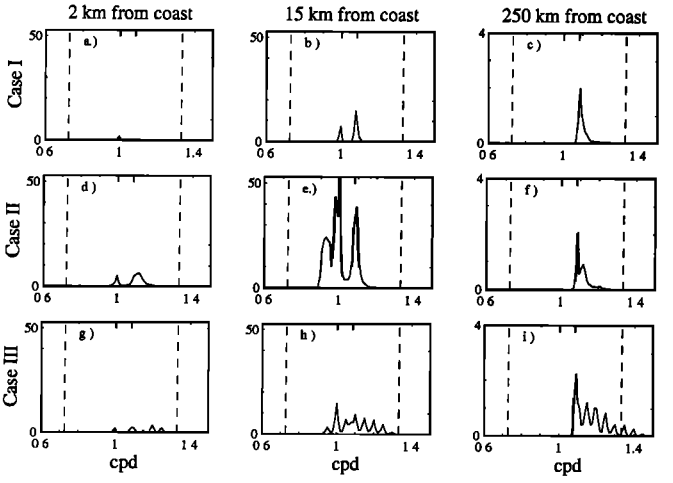

Figure 17. Vertically averaged, clockwise rotary spectra of the currents from the model simulations. Counterclockwise variances were 2-3 orders of magnitude lower than clockwise variances. The alongshore jet modulation for (a-c) simulation case I, (d-f) case II, and (g-i) case III is shown in Figures 16d-16f. Spectra are shown for three different locations from the coast. The vertical dashed lines mark the range of the diurnal band of this study (0.727-1.33 cpd). The thick solid lines at the top of each panel mark the diurnal (left line) and inertial (right line) frequencies. Note that the scale of the spectra of the currents 250 km from the coast is different than for the other two cross-shore locations.

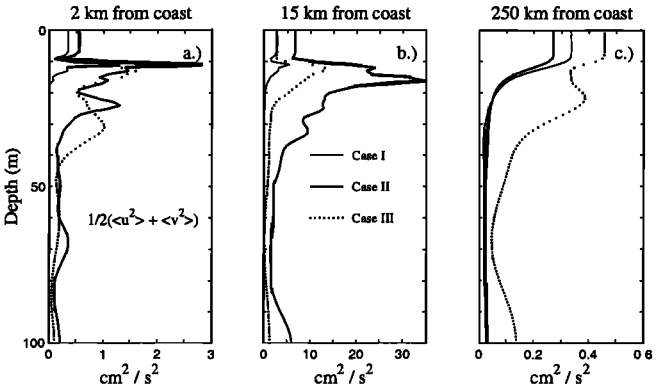

Figure 18. Kinetic energy versus depth from time-dependent simulations at (a) 2 km, (b) 15 km, and (c) 250 km from the coast. For all three cases, the kinetic energy was averaged over the period between days 50 and 150 of the simulations (the time period when the jet was turned on). Note that the kinetic energy scales of Figures 18a-18c are different.

terclockwise variance (not shown in Figure 17) was 2-3 orders of magnitude lower than clockwise variance. Clockwise spectral levels were low at 2 km from the coast. In case I, there was a peak at the diurnal frequency and a smaller one at the inertial frequency. In case II, there was a broad inertial peak and a somewhat smaller and narrower diurnal peak. In case III, variance was more evenly distributed from the diurnal frequency to the upper bound of the diurnal band.

At 15 km in case I, there were two distinct peaks at the diurnal and inertial frequencies. The inertial peak was larger than the diurnal peak despite the considerably stronger forcing at the diurnal frequency (the diurnal wind peak was much larger than the background level at f, Figure 9a). The near-resonant response of the ocean at f, apparently, caused the large response despite the weak forcing. Not surprisingly, the 15 km spectrum was much more energetic for case II. The largest peak in CW variance was at the diurnal frequency, but an inertial peak was only slightly smaller. Variance was also apparent at frequencies lower than σ_{D_i} and higher than f. In case III, energy was also highest at the diurnal frequency. However, the variance was broadly distributed between σ_{D_i} and the upper bound of the diurnal band.

The scales of the spectra for the 250 km cross-shore location are expanded relative to the spectra from the locations closer to shore. Here, beyond the direct influence of the wind and the jet, variance was at and higher than the inertial frequency. This was apparently due to slightly superinertial internal waves radiating away from the coast. This near-inertial variance was highest in case III, the case in which V was modulated with the shortest timescale.

Horizontal kinetic energy versus depth is plotted for the three cases in Figure 18. The kinetic energy was averaged over the time period between days 50 and 150 of the simulations, the period when the jet was turned on in cases II and III. In all three cases, KE was highest at 15 km from the coast (note that the KE scales of Figures 18a-18c are different). In case I, KE at 15 km from the coast was low and was confined to the mixed layer and slightly below. In case II, KE was considerably greater than in case I. A maximum occurred below the mixed layer at a depth of $\sim$ 16 m. Most of the KE was confined to the upper 40 m of the water column, but some energy was present down to the seafloor. Energy was present below the mixed layer in case III but did not penetrate as deeply as in case II. A small amount of KE was present at the seafloor.

7. Discussion

Despite its simplicity, the model that we have presented demonstrates that background currents can be important in regulating the degree to which the sea breeze can pump energy into the coastal ocean. The model predicts that at a latitude of 32.75°, little diurnal energy would be pumped into the ocean without the presence of a negative background vorticity. Even with a constant diurnal forcing by the wind, a time varying background flow can produce an ocean response that is highly intermittent.

The model diurnal-band currents resembled the currents observed during IWAVES. Both were predominantly clockwise polarized. During IWAVES, currents near the coast ($H < 30$ m) were elliptical and oriented in the alongshore direction, whereas currents farther offshore were circularly polarized. In the model the polarization is dependent on Γ and, consequently, offshore distance ($|v|/|u| = \Gamma f/\sigma$, (16)). In order for the model to explain the polarization pattern observed during IWAVES, Γ would need to be consistently > 1 ($V_x > 0$) near the coast. For example, for the values of ϵ^{-2} typically observed at the 15-30 m moorings ($\sim$ 0.4, Table 3), Γ would need to be $\sim$ 1.5. However, this probably did not occur during IWAVES because V could be either northward or southward, and since these currents typically decayed toward the coast, V_x near the coast could be either positive or negative and was probably not consistently > 0. Thus the cross-shore dependence of polarization observed during IWAVES cannot be explained by the model.

Both during IWAVES and in the model, diurnal-band KE was highest near the surface of the water column and decayed with depth. However, the model had maximum KE below the mixed layer which was not typically observed during IWAVES , except at the 500 m mooring in the summer of 1997 (Figure 4c), where a maximum in KE occurred at a depth of 37 m.

Diurnal-band variance increased from the coast to 10 km offshore during IWAVES as well as in the model (Figures 4 and 14, respectively). In the model this was a consequence of the coastal boundary condition ($u = 0$ and, consequently, $v = 0$ because of (6)) and the cross-shore profile chosen for Γ (Figure 15b), which was always $> \sigma^2/f^2$ at the coast ($|x| < 5.4$ km) and did not allow significant diurnal motions to be driven there (Figure 15c).

At 15 km from the model coast, current spectra from the model were much broader than the spectrum of the wind, as was observed during IWAVES. The broadening in the model apparently was caused by the slow changes in V,

which allowed for frequency mixing. The slow changes in V also caused the cross-shore location of the caustics (location where $\Gamma = \sigma^2/f^2$) to change over time, further complicating the temporal and spatial response of the ocean.

In the summers of 1996 and 1997, diurnal-band KE appeared to be enhanced when $\Gamma < \sigma^2/f^2$ (Figures 6 and 8). However, in the fall of 1996, KE at the 100 m mooring appeared to be greatest when $\Gamma > 1$ (Figure 7). This discrepancy between the model and the IWAVES observations may have been caused by several factors. First, the model may not contain all the relevant physics necessary to describe the diurnal intermittency observed during IWAVES. We will address this in more detail below. Second, the finite difference estimate of V_x between the 100 and 30 m moorings may not have been representative of the true relative vorticity at the 100 m mooring. The low-frequency currents at the 30 m mooring were weak and, for the purpose of estimating V_x, effectively zero. Thus, when V at the 100 m mooring was negative, the estimate of V_x was positive, and when V at the 100 m mooring was positive, V_x was negative (Figure 7). When moorings farther offshore were used to estimate V_x, however, the opposite could occur. For example, in the summer of 1997 between days 205 and 213 (Figure 8b), V was negative at the 120, 350, and 500 m moorings, and a positive V_x would have been estimated if the finite differencing was done between one of these moorings and the 30 m mooring. However, V was most negative at the 120 m mooring and least negative at the 500 m mooring, and the resultant V_x was negative.

The idealized, flat-bottomed model most likely does not contain all the physics that contributed to the complicated diurnal currents observed during IWAVES. The influence of a sloping bottom on the propagation of the diurnal internal waves was not taken into account. However, since most of the diurnal energy was concentrated in the upper portion of the water column, the internal waves probably radiated out of the IWAVES study site before reflecting off the bottom. Therefore the sloping bottom in the vicinity of the study site may not be relevant.

Dissipation was also ignored. Again, this is probably not a problem in the region where the diurnal motions were directly forced by the winds (e.g., the entire IWAVES study site) since most of the energy is near the surface and not subjected to bottom friction. However, the distant response of the model (far away from the sea breeze forcing) is probably not realistic because the waves will lose energy as they propagate away from their source.

In addition, there was no alongshore dependence in the model. If there was alongshore dependence in the diurnal winds during IWAVES, subinertial diurnal Kelvin waves could have been generated. These waves would propagate northward up the coast and may have intermittently entered the IWAVES study site. Alongshore dependence in V could have caused diurnal energy to be advected into or out of the study site.

Low-frequency currents were often vertically sheared during IWAVES, but the model assumed the background jet was barotropic. Since V was often baroclinic, cross-shore gradients in density must have been present. *Hayes and Halpern* [1976] showed that cross-shore gradients in density can modify the internal wave dispersion relationship. In the presence of an alongshore geostrophic current, internal waves can freely propagate within the frequency range $(f^2\Gamma - M^4/N^2)^{1/2}$ and N, where $M^2 = -g\rho_x/\rho_o$. When $M = 0$, free internal waves can exist when $\Gamma < \sigma^2/f^2$ (the relevant relationship in the model presented here). The presence of a cross-shore gradient in ρ, however, will modify this relationship. Whether M^2 is positive or negative, it will tend to reduce the lower limit of the free internal wave band. Thus slow changes in cross-shore density gradients, in addition to the vorticity of the background currents, could have changed the effective Coriolis parameter at the IWAVES study site and contributed to the intermittent behavior of the observed diurnal currents.

Acknowledgments. The IWAVES field program and subsequent analysis effort has been funded by the Office of Naval Research. The authors wish to thank Lou Goodman for his support of this project. We also thank Charles Coughran, Paul Harvey, and Jerry Wanetick for their help in mooring development and deployment, instrument maintenance, data collection and maintenance, and computer support. Thanks also to Clive Dorman, who provided help in interpreting the wind data, and to Dave Chapman for his careful review of the manuscript.

References

Baines, P. G., Internal tides, internal waves and near-inertial motions, in *Baroclinic Processes on Continental Shelves, Coastal Estuarine Sci.*, vol. 3, edited by C. N. K. Mooers, pp. 19–31, AGU, Washington, D. C., 1986.

Balmforth, N. J., S. G. Llewellyn-Smith, and W. R. Young, Enhanced dispersion of near-inertial waves in an idealized geostrophic flow, *J. Mar. Res.*, *56*, 1–40, 1998.

Balmforth, N. J., and W. R. Young, Radiative damping of near-inertial oscillations in the mixed layer, *J. Mar. Res.*, *57*, 561–584, 1999.

D'Asaro, E. A., Wind forced internal waves in the north Pacific and Sargasso Sea, *J. Phys. Oceanogr.*, *14*, 781–794, 1984.

D'Asaro, E. A., Upper-ocean inertial currents forced by a strong storm, part III, Interaction of inertial currents and mesoscale eddies, *J. Phys. Oceanogr.*, *25*, 2953–2958, 1995.

D'Asaro, E. A., C. C. Eriksen, M. D. Levine, P. Niiler, C. A. Paulson, and P. Van Meurs, Upper-ocean inertial currents forced by a strong storm, part I, Data and comparisons with linear theory, *J. Phys. Oceanogr.*, *25*, 2909–2936, 1995.

Denbo, D. W., and J. S. Allen, Rotary empirical orthogonal function analysis of currents near the Oregon coast, *J. Phys. Oceanogr.*, *14*, 35–46, 1984.

Dorman, C. E., Winds between San Diego and San Clemente Island, *J. Geophys. Res.*, *87*, 9636–9646, 1982.

Gill, A. E., and A. J. Clarke, Wind-induced upwelling, coastal currents and sea-level changes, *Deep Sea Res.*, *21*, 325–345, 1974.

Hayes, S. P., and D. Halpern, Observations of internal waves and coastal upwelling off the Oregon coast, *J. Mar. Res.*, *3*, 247–267, 1976.

Kundu, P. K., An analysis of inertial oscillations observed near Oregon coast, *J. Phys. Oceanogr.*, *6*, 879–893, 1976.

Kunze, E. L., Near-inertial wave propagation in geostrophic shear, *J. Phys. Oceanogr.*, *15*, 544–565, 1985.

Kunze, E. L., and T. B. Sanford, Observations of near-inertial waves in a front, *J. Phys. Oceanogr.*, *14*, 566–581, 1984.

Leaman, K. D., Observations on the vertical polarization and en-

ergy flux of near-inertial waves, *J. Phys. Oceanogr., 6*, 894–908, 1976.

Lerczak, J. A., Internal waves on the southern California shelf, Ph.D. thesis, Univ. of Calif., San Diego, La Jolla, 2000.

Lindzen, R. S., and H.-L. Kuo, A reliable method for the numerical integration of a large class of ordinary and partial differential equations, *Mon. Weather Rev., 97*, 732–734, 1969.

van Meurs, P., Interactions between near-inertial mixed layer currents and the mesoscale: The importance of spatial variabilities in the vorticity field, *J. Phys. Oceanogr., 28*, 1363–1388, 1998.

Zervakis, V. and M. D. Levine, Near-inertial energy propagation from the mixed layer: Theoretical considerations, *J. Phys. Oceanogr., 25*, 2872–2889, 1995.

M. C. Hendershott and C. D. Winant, Center for Coastal Studies, 0209, Scripps Institution of Oceanography, La Jolla, CA 92093-0209 (mch@coast.ucsd.edu; cdw@coast.ucsd.edu)

J. A. Lerczak, Department of Physical Oceanography, MS#21, Woods Hole Oceanographic Institution, Woods Hole, MA 02543 (jlerczak@whoi.edu)

(Received January 25, 2001; revised June 14, 2001; accepted June 14, 2001.)